Ocean Modelling 182 (2023) 102176

Contents lists available at ScienceDirect

Ocean Modelling

journal homepage: www.elsevier.com/locate/ocemod

Extreme cooling of 12.5 °C triggered by Typhoon Fungwong (2008)

Zhe-Wen Zheng [a,*], Jia-Yi Lin [a], Ganesh Gopalakrishnan [b], Yi-Rui Chen [a], Doon-Jing Doong [c], Chung-Ru Ho [d], Quanan Zheng [e], Chau-Ron Wu [a], Chen-Fen Huang [f]

[a] Institute of Marine Environmental Science and Technology & Department of Earth Science, National Taiwan Normal University, Taipei, Taiwan
[b] Climate Atmospheric Science and physical Oceanography, Scripps Institution of Oceanography, La Jolla, CA, USA
[c] Department of Hydraulic and Ocean Engineering, National Cheng Kung University, Tainan, Taiwan
[d] Department of Marine Environmental Informatics, National Taiwan Ocean University, Keelung, Taiwan
[e] Department of Atmospheric and Oceanic Science, University of Maryland, College Park, MD, USA
[f] Institute of Oceanography, National Taiwan University, Taipei, Taiwan

ARTICLE INFO

Keywords:
Typhoons
Kuroshio intrusion
Sea surface temperature
Moored buoy
Numerical modeling
Float trajectory

ABSTRACT

Typhoon Fungwong, a category-2 but deadly typhoon in the 2008 Pacific typhoon season, made landfall first on Taiwan and then on Southeast China. During its approach toward Taiwan, it triggered an extreme sea surface temperature (SST) drop of 12.5 °C, which was the strongest SST drop recorded by Longdong buoy northeast of Taiwan coast from 1998 to 2017. In this study, including moored buoy temperature measurements, Argo float temperature profiles, satellite-observed SSTs, and a suite of numerical experiments performed using the Regional Ocean Modeling System were used to unveil the detailed processes of how Fungwong triggered such an extreme cooling. Subsequently, the source of the cold waters feeding the extreme cooling, possible mechanisms triggering the cooling, and consequential effects of cooling on the ambient ocean environment were systematically investigated. Results show that the extreme cooling was triggered mainly by a process of uplift of subsurface cold water tied to shore-ward Kuroshio intrusion driven by easterly/northeasterly winds and consequential entrainment mixing, while coastal upwelling driven by persistent longshore (southerly) winds plays a minor role. Nevertheless, the southerly winds still help the enhancement of entrainment mixing and thus the sea surface cooling. Finally, modeled float trajectories with temperature tracers identified where the cold water goes and indicate that the temperature drop might extend all the way toward the south end of Japan (Kyushu) along the flowing path of Kuroshio.

1. Introduction

Sea surface temperature (SST) variability triggered by tropical cyclone (TC) passages, which might affect regional weather system, oceanic environment, ecosystems, fisheries, and typhoon characteristics, attracts considerable attentions from the oceanic, atmospheric, metrological and even climatological communities (Cione and Uhlhorn, 2003; Lin et al., 2003; Babin et al., 2004; Siswanto et al., 2007; Morimoto et al., 2009; Zheng et al., 2010, 2015; Kuo et al., 2017; Mohanty et al., 2019). For long, warm ocean has been considered an energy source for TC development (Schade and Emanuel, 1999; Shay et al., 2000; Wu et al., 2007; Lin et al., 2008). In other words, upper ocean temperature variations in response to TC–ocean interaction ahead or just behind the passage of the eye-center play a key role in TC intensity development (Schade and Emanuel, 1999; Lee and Chen, 2014; Zheng et al., 2015; Glenn et al., 2016; Kuo et al., 2018).

In addition to possible feedback to TC intensity, TCs have also been shown to play a key role affecting the regional ocean environment. Morimoto et al. (2009) showed that typhoon passages not only pushed the Kuroshio axis shelf-ward but also enhanced the intensity of the Kuroshio east of Taiwan. Zheng et al. (2014) showed the marked Kuroshio modulation in response to the passage of typhoon Morakot (2008). In addition, typhoon Morakot also triggered a cooling response of more than 4 °C off the southeast corner of Taiwan that was advected along the Kuroshio east of Taiwan toward northeast of Taiwan (Kuo et al., 2017). By contrast, on the basis of numerical experiments, Zheng et al. (2017) indicated that the strong local wind off northeast Taiwan carried by TC passage might drive the Kuroshio shore-ward and cause marked cooling over the East China Sea (ECS) continental shelf. An air–sea coupling model study by Kuo et al. (2018) focused on the interaction between TC and the Kuroshio in the Luzon Strait. They reported an unexpected movement of subsurface frontal structure in the Luzon Strait, which later resulted in a 3 °C –4 °C sea surface cooling and subsequent reduction of TC intensity. This negative feedback resulting from the TC–Kuroshio interaction to TC intensity contradicts the former

* Corresponding author.
E-mail address: zwz@ntnu.edu.tw (Z.-W. Zheng).

https://doi.org/10.1016/j.ocemod.2023.102176
Received 24 June 2022; Received in revised form 23 December 2022; Accepted 31 January 2023
Available online 3 February 2023

concept that warmer Kuroshio waters would favor the development of TC passing over it.

Recently, Doong et al. (2019) investigated typhoon-induced SST cooling in the coastal region by continuous moored buoy observations. They indicated that typhoon Fungwong (2008) induced an extreme cooling reaching up to 12.5 °C, which is the maximum SST drop ever recorded by moored buoy deployed at Longdong from 1998 to 2017. On the basis of indirect evidences, they concluded that the strong and persistent longshore (southerly) winds inducing coastal upwelling might be the dominant cause leading to the extreme SST drops surrounding Longdong. This extreme cooling occurred at the flowing path where Kuroshio passes through. Thus, the cold-water pulses might get advected all the way down to the Kuroshio downstream region and cause threats along its path, such as a number of physiological, behavioral, and fitness-related consequences for fish, termed as cold-shock stress (Donaldson et al., 2008; Troy et al., 2012; Kuo et al., 2017). Additionally, given its extraordinary strength, this cooling response to Fungwong largely attracts our attention.

In this study, moored buoy measurements of temperature, Argo float temperature profiles, satellite-observed SST, and a series of numerical experiments using the Regional Ocean Modeling System (ROMS) were applied to resolve the detailed progress of how the TC Fungwong triggers such an extreme cooling. Observed temperatures retrieved from three different methodologies were integrated to validate model-simulated temperature responses in different regions at different spatial scales. Simulated floats trajectories with temperature tracers were used to answer the question of where the cold water goes. Overall, the source of the cold waters feeding this extreme sea surface cooling, the possible mechanisms triggering it, and the consequential effects sourcing from the cooling on the surrounding oceanic environment were systematically investigated.

2. Data and methods

2.1. Satellite SST

In this study, daily microwave optimally interpolated SST merged from Tropical Rainfall Measuring Mission (TRMM) Microwave Imager (TMI), the Advanced Microwave Scanning Radiometer (AMSR-E), and WindSat Radiometer were used to quantify the offshore sea surface cooling to TC Fungwong passage under all weather conditions. The spatial resolution of this gridded SST product is 0.25 degree. This merged product was processed and distributed by Remote Sensing Systems through http://www.remss.com/measurements/sea-surface-temperature/oisst-description/. In addition to pure microwave sensor merged product, multiscale ultrahigh resolution SST (MURSST) was also collected for cross analysis, especially for the coastal regions. This product was processed as a global, gap-free, gridded, daily 1 km SST by merging infrared data from the advanced-very-high-resolution-radiometer (AVHRR), Moderate Resolution Imaging Spectroradiometers (MODIS), and microwave data from AMSR-E and AMSR-2, as well as in-situ SST observations from the NOAA iQuam project (Chin et al., 2017). MURSST data were processed and released by NASA Jet Propulsion Laboratory, Physical Oceanography Distributed Active Archive Center (PO. DAAC) through https://podaac.jpl.nasa.gov/.

2.2. In-situ temperature

SST can be measured either by satellite-based remote sensing techniques or in-situ measurements from ships, floats, or moored buoys (Matthews, 2013; Doong et al., 2019). Moored buoys record continuous and long-term time series of the SST at certain site. Here, the long-term SST measurement record located at Longdong coast was provided by a 2.5 m discus-shaped moored buoy, which was deployed by the Coastal Ocean Monitoring Center of National Cheng Kung University in 1998 (Doong et al., 2019). This buoy is approximately 0.6 km off the Longdong coast and is situated in the water at a depth of 23 m. The buoy is anchored to the sea bottom. The SST was measured by a platinum resistance temperature detector, which can cover a range of −10° C–70° C and installed at 0.6 m below the sea surface. Further description about the moored buoy data can be seen in Doong et al. (2019). In addition, the long-term buoy-measured SSTs covering the period from 1998 to 2017 can be accessed through https://doi.org/10.1594/PANGAEA.895002.

2.3. Ocean model description and experiment design

Relative to sparse observations provided by either moored buoy temperature meter at certain site or satellite snapshots, model simulation usually plays an important role in improving the continuous understanding of certain physical process. To understand the detailed progress of upper ocean variability surrounding Longdong to the passage of TC Fungwong, regional ocean circulation was simulated by the ROMS model here. The ROMS is a relatively new generation ocean circulation model that has been applied to multidisciplinary ocean modeling research; it is a free-surface, primitive equation, curvilinear coordinate oceanic model. Barotropic and baroclinic momentum equations in ROMS are separately resolved. Meanwhile, a non-local, K-profile planetary boundary layer scheme (Large et al., 1994) was applied to parameterize the subgrid-scale mixing processes in the vertical. In addition, to have a higher spatial resolution for resolving the small-scale circulation features surrounding Longdong and a larger model domain for resolving the large-scale circulation features including the whole progress corresponding to TC Fungwong passage from open ocean toward onshore region simultaneously, a multilevels nested-grid ROMS was implemented.

The parent model with a horizontal resolution of approximately 7 km covered the region from 17° to 30° N and from 116° to 133° E (Fig. 1), and the nested model with a horizontal resolution of approximately 2 km covered the region from 21.7° to 26.2° N and from 120.4° to 123.5° E. Given that the buoy measured temperature sourcing mainly from a large amount of offshore water temperature (will be demonstrated in following analyses), thus, a 2-km spatial resolution was considered good enough to reproduce the processes leading to the extreme cooling. The vertical gridding of the parent and nested models consists of 20 s-coordinate levels (theta_s = 6, theta_b = 0, Hc = 10) that were unevenly distributed for better resolution of the upper ocean relative to that of bottom layer or lower layers (Song and Haidvogel, 1994). Model bathymetry was created by merging regional bathymetry of 500-m spatial resolution, processed and distributed by Ocean Data Bank (ODB) sponsored by the Ministry of Science and Technology, Taiwan, and etopo2 global ocean bottom topography (Smith and Sandwell, 1997). Additionally, the model was driven by momentum forcing from hourly sampled gridded (0.5-degree latitude x 0.625-degree longitude) Modern-Era Retrospective analysis for Research and Applications, version 2 (MERRA-2) winds (https://disc.gsfc.nasa.gov/), which is one of the most up-to-date wind forcing products. The comparison between winds retrieved from in-situ measurement and MERRA-2 from July 24 to 31 can be seen in Figure S1 in supplementary online materials (SOM). Generally, MERRA-2 winds show consistent patterns as the winds measured by the weather buoy (fixing to 10 m height using the log-law model (Manwell et al., 2009)). Therefore, the wind product was deemed to be reasonable to drive ROMS.

By contrast, atmospheric fields retrieved also from MERRA-2, including air temperature, relative humidity, precipitation rate, incoming shortwave radiation, and outgoing longwave radiation (0.5-degree latitude x 0.625-degree longitude), were integrated for calculating net heat flux across the air–sea interface, which consequently influenced the SST variability. The model initial conditions and lateral boundary conditions were derived from the data-assimilated HYbrid Coordinate Ocean Model (HYCOM) global solutions with 1/12-degree spatial resolution through https://www.hycom.org/dataserver/gofs-3pt1/

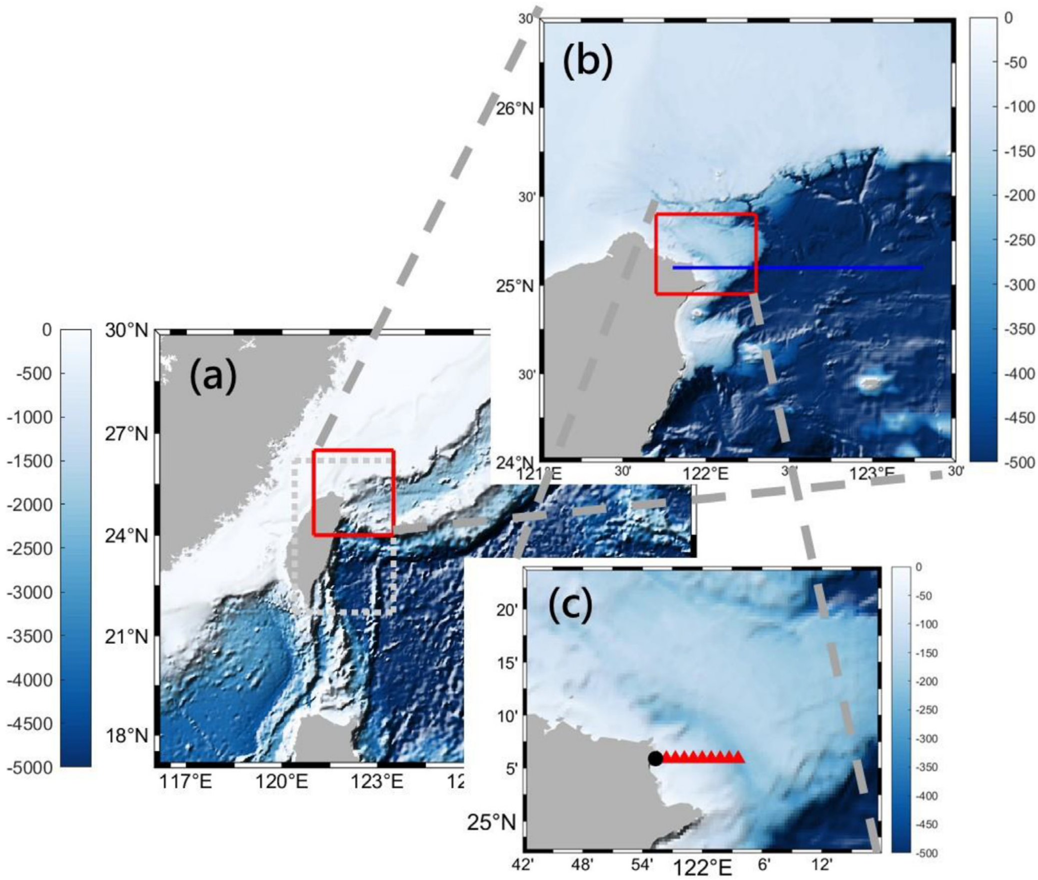

Fig. 1. (a) Complete study area and (b, c) the areas zoom-in toward to Longdong site. Blue line in (b) extending 150 km offshore denotes the transect for capturing the variability of the KMS surrounding this region (will be shown in Fig. 6). Black dot in (c) denotes the location of Longdong weather buoy. Red triangles in (c) mark the location of the release of modeled floats. Gray dotted lines in (a) denote the nested (children) model domain.

reanalysis (Cummings, 2005). For the Fungwong study, model simulations were executed from July 19 to July 31 (August 5 for trajectories analysis), 2008. Temporal frequency of the model is 5 min, and the output frequency is 1 h. In addition, first three days' outputs of individual simulations are excluded in following analyses for avoiding possible insufficient spinning up of smaller scale features in the inner domain. Detailed description of ROMS is given by Shchepetkin and McWilliams (2003, 2005). Related validations of the model skill for storm simulations can be seen in Zheng et al. (2010, 2014) and Shen et al. (2021). Fig. 2 shows the systematic comparison of temperature variations retrieved from all available Argo floats passing the study area during the Fungwong passage and corresponding ROMS model simulations (Positions of the floats used for the evaluation can be seen in Figure S2 in SOM).

3. Extreme cooling response to fungwong

3.1. Satellite observations

Fig. 3(a–e) shows the cooling responses derived from satellite observations of TMI/AMSR-E/WindSat gridded SST. As the typhoon Fungwong progresses westward on 26 July, it starts affecting the upper ocean temperature and causes a near-surface cooling of about 3 °C centered at 22° N, 129° E. Afterward, the cold-water patch grows to stronger cooling response with an SST drop of more than 4 °C relative to the state of pre-typhoon passage. Subsequently, the main offshore cooling (surrounding 20° N–23° N, 126° E–129° E) triggered by Fungwong starts to weaken on 28 July. At the same time, Fungwong leads to a marked cooling on the ECS shelf region off northeast Taiwan. On 29 July, cooling at nearshore and offshore regions strengthens and weakens, respectively. Afterward, offshore and nearshore coolings decrease gradually until August 5 (figure not shown), recovering to the state of pre-typhoon passage.

3.2. ROMS simulations

Fig. 3(f–j) shows the corresponding cooling progress during July 26–30, 2008 from model simulations. Overall, simulations reproduce the satellite-observed cooling progress reasonably well, with respect to the timing and location of the cold-water patches, despite inconsistent of time averaging for composite SST image and model simulation, leading to minor difference between modeling and remote sensing (Ko et al., 2016). However, in the nearshore region, satellite-observed SST shows much weaker cooling relative to simulated SST. Brewin et al. (2017) compared SST derived from AVHRR with SST collected by in-situ instrument at coastal and offshore regions, respectively. They indicated that the lower performance of satellite-based SST at the coastal region when compared with offshore waters. This result could serve as a possible reason for the discrepancy in our comparison between model simulations and satellite observations at the shelf region.

3.3. Moored buoy temperature measurements

Fig. 4 shows direct measured temperature of approximately 12.5 °C cooling at 0.6 m below the sea surface (red line) by the moored buoy temperature meter deployed at Longdong (25.0983° N, 121.9219° E, black dot in Fig. 1), together with model-simulated SST (blue line) and satellite-observed SST (gray-dashed line) during the passage of Fungwong. Here, MURSST data were used in the comparison because merged microwave data are absent in the nearshore region. Model

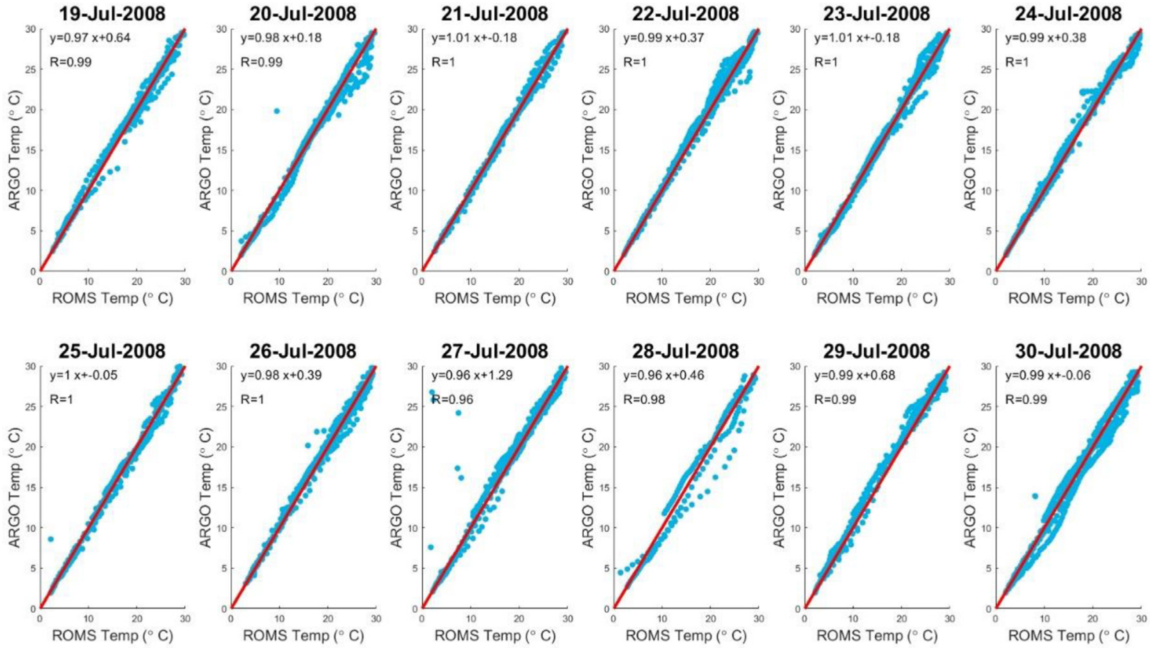

Fig. 2. Comparison of temperatures derived from in-situ ARGO float measurements and ROMS model simulations during typhoon Fungwong passage. Correlation coefficients between in-situ ARGO and ROMS temperatures are statistically significant (with all P-values < 0.05).

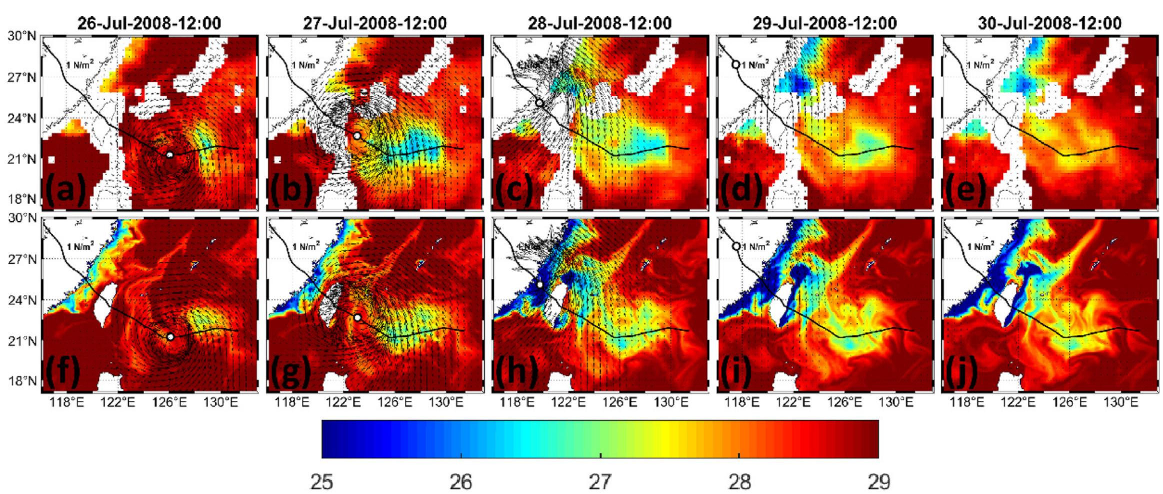

Fig. 3. (a–e) Satellite observations of TMI/AMSR-E/WindSat SST and (f–j) model simulated SST cooling in response to the passage of TC Fungwong from 26–30 July 2008. Color shadings denote SST cooling (in °C). Wind stress (N/m^{-2}) calculated from MERRA-2 during typhoon passage were superimposed on the SST fields. Hollow circles denote the central positions of Fungwong.

simulations show relatively good skill in resolving the temporal variation of near-surface temperature. By contrast, MURSST at nearshore regions largely underestimates and almost fails to capture the cooling feature in response to progression of Fungwong. The result shows again the disadvantage of satellite observations for monitoring temperature surrounding shelf regions. Same conclusion can be seen in Woo and Park (2020). Their results emphasized the importance of using real-time in-situ measurements as much as possible to overcome the increasing SST errors in coastal regions. Nevertheless, for offshore regions, satellite observations still provide reliable SST measurements (Brewin et al., 2017; Woo and Park, 2020), which can help validate model simulations at different regions.

3.4. Detailed progression of strong cooling surrounding longdong

Fig. 5 (a–e) shows the simulated progress of Fungwong triggered extreme sea surface cooling surrounding Longdong off northeast Taiwan. The sea surface cooling starts at 06:00 on July 28 with a temperature drop of approximately 6 °C relative to surrounding regions (Fig. 5c). Cooling appears just for a while when wind direction changes from due east to southeast. This phenomenon shows a marked discrepancy about the timing of the generation of cooling response relative to the findings by Doong et al. (2019), which suggested that the presence of strong and persistent southerly winds, inducing coastal upwelling, is the dominant cause for the extreme cooling surrounding Longdong. Later, the cooling grows sharply and extends northeastward with an SST drop of more than 10 °C. Meanwhile, an SST drop of over 10 °C covers an area of up to 2,500 square kilometers (Fig. 5d).

Examining the state below the sea surface provides additional information about the generation of sea surface cooling. Fig. 6 shows transects of temperature (in color shadings), currents (white arrows denoting vectors of u and w × 10^3), the position of subsurface cold water (denoted by 20 °C isotherms in bold red contours), as well as the position where the Kuroshio mainstream (KMS) passes through

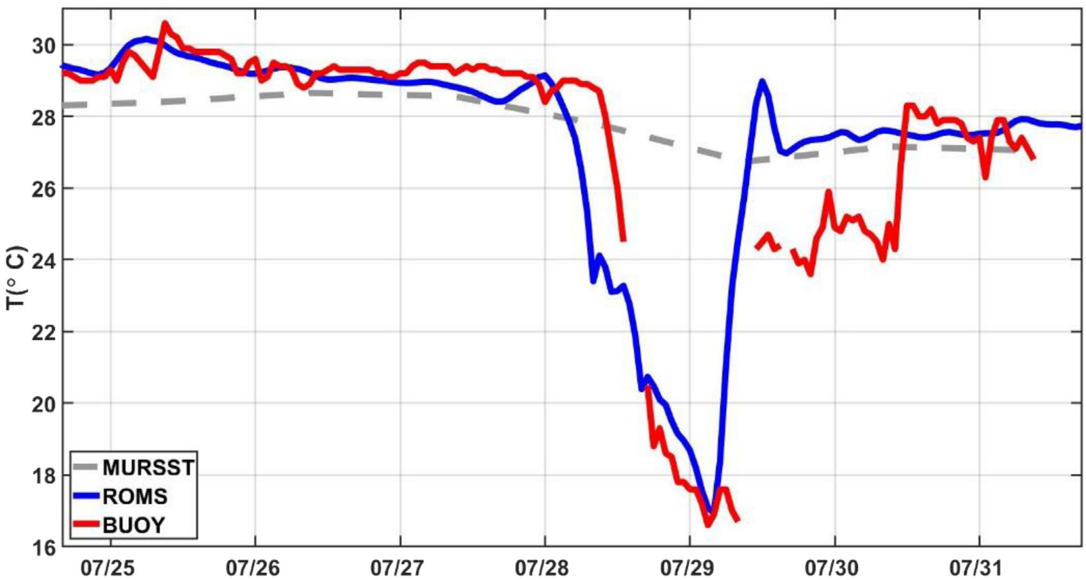

Fig. 4. The significant near-surface temperature drops in response to the passage of Fungwong in July 2008. Red, gray-dashed, and blue lines denote the temperature variabilities derived from moored buoy temperature meter (installed at 0.6 m depth), satellite-observed MURSST, and model-simulated SST (temperature at 0 m depth).

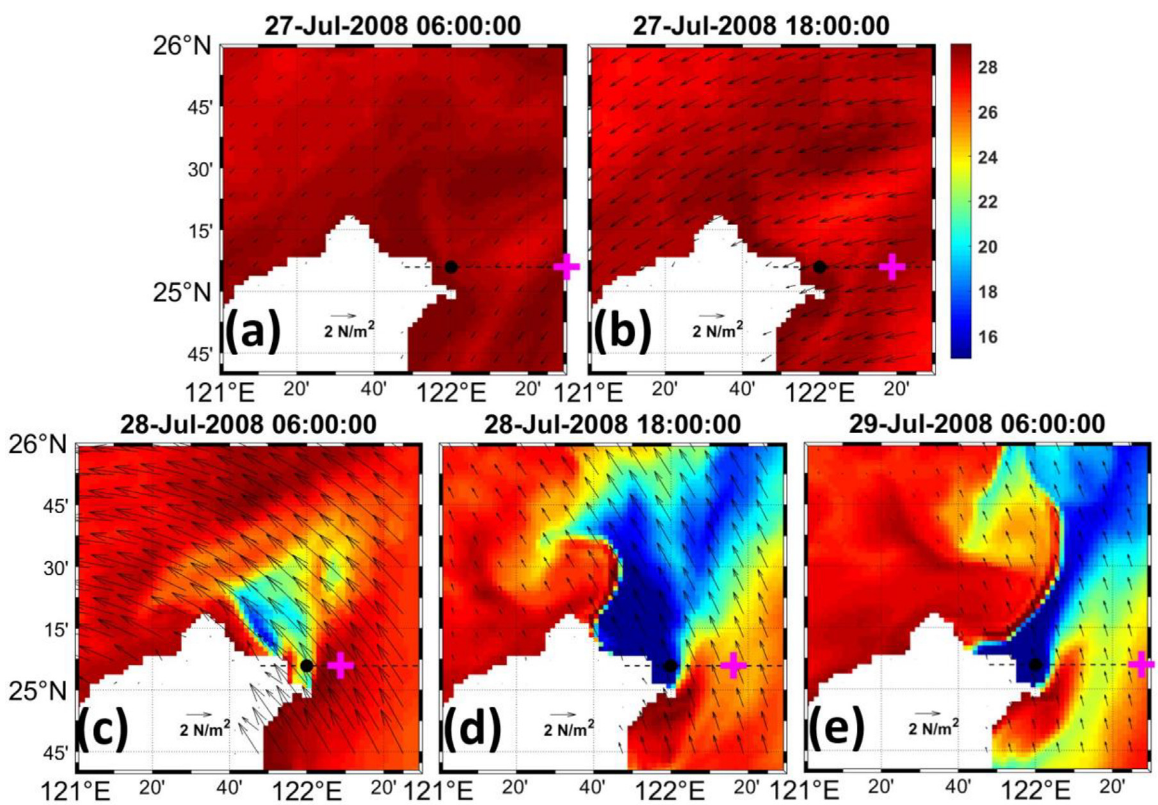

Fig. 5. (a–e) Regional SST cooling responses (°C, color shading) during Fungwong passage from 27 July 06:00 to 29 July 06:00. Black arrows denote corresponding wind stress (unit: Nm^{-2}). Black dots mark the position of 122 °E, 25.08 °N. Black dashed lines denote the latitudinal transects (along 25.098 °N) appeared in Fig. 6. Pink plus signs mark core positions of KMS along 25.098 °N. The core position was defined by maximum northward current speed (average between 0–50 m) along the 25.098 °N transect.

during the Fungwong passage. The position of KMS was defined by outlines with northward current speeds greater than 70 cm s^{-1} (in black contours, contour intervals are 20 cm s^{-1}). Bold-black contours denote current speed equal to 110 cm s^{-1}. Pink plus signs mark core positions of KMS along 25.098 °N. The core position was defined by maximum northward current speed (average between 0–50 m) along the 25.098 °N transect. First, in reference to the variation of KMS, the current core of Kuroshio moves shoreward from 06:00 on July 27 to 06:00 on July 28 (see Fig. 6a–6c) and then gradually retreats toward offshore back to the original position from 18:00 on July 28 to 06:00 on July 29 (6d–6e).

Subsequently, in reference to the variations of subsurface cold water, with the Kuroshio intrusion onto the shelf, the subsurface cold-water uplifts markedly from 18:00 on July 27 to 18:00 on July 28 (6b–6d). The dynamic linkage between onshore-ward Kuroshio intrusion and uplift of subsurface cold water can be explained by the

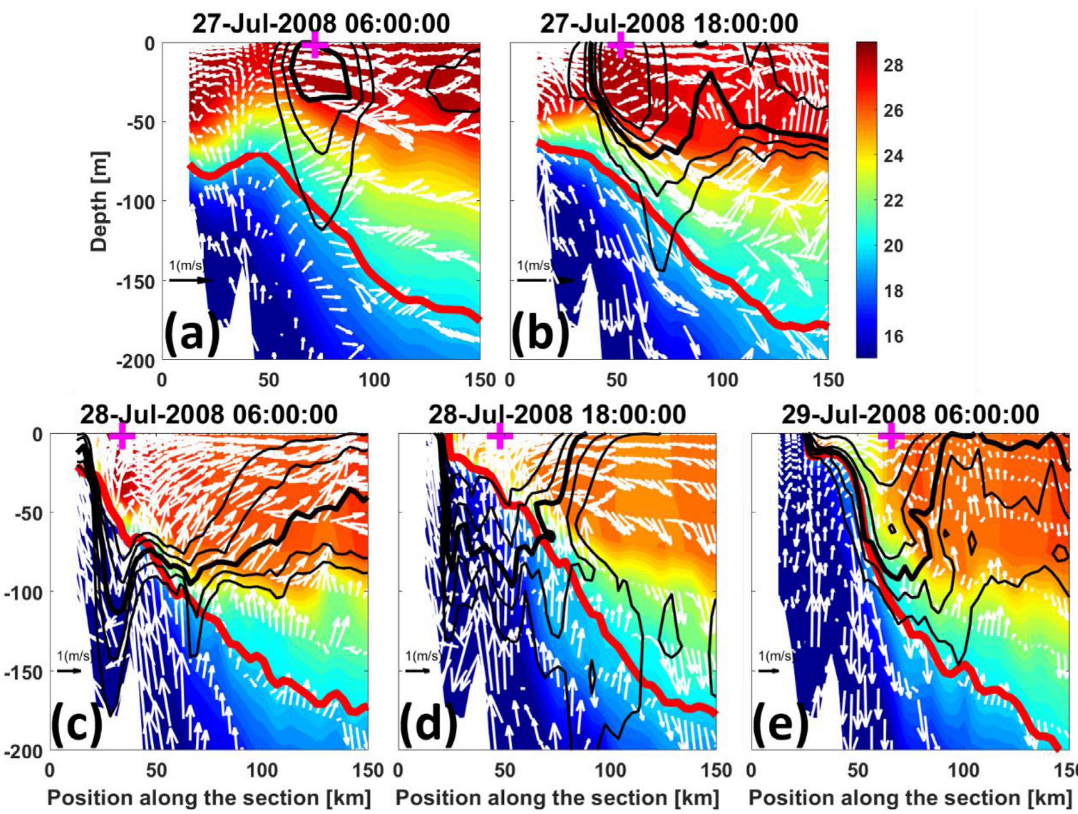

Fig. 6. (a–e) Latitudinal transects (from 121.8 °E to 123.3 °E, along 25.098 °N) of temperature (°C, color shading), velocities (u and w × 10^3, in white arrows), as well as the position where KMS passing through during Fungwong passage. The position of KMS was defined by outlines with northward current speeds greater than 70 cm s^{-1} (in black contours, contour intervals are 20 cm s^{-1}). Bold-black contours denote current speed equal to 110 cm s^{-1}. Pink plus signs mark core positions of KMS along 25.098 °N, as shown in Fig. 5. Bold-red contours denote 20 °C isotherms.

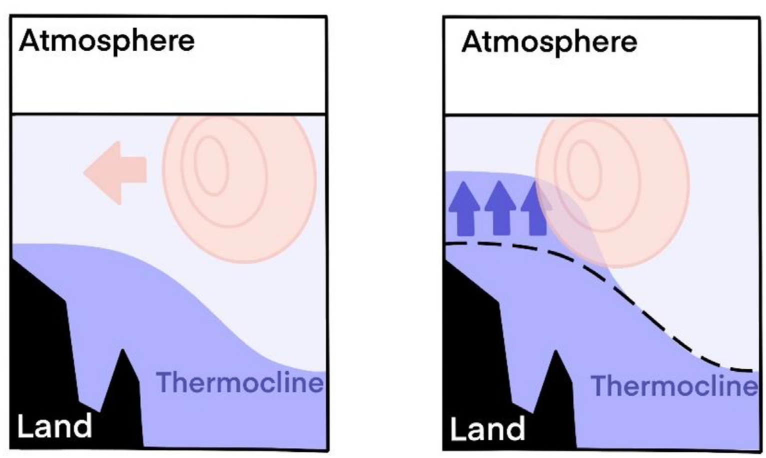

Fig. 7. According to Tomczak and Godfrey (1994), the uplift (dark blue arrows) is a result of the thermocline slope across a current. Temperature field reacts to the presence of a strong current by adjusting to geostrophic equilibrium. Meanwhile, because isotherm depths offshore-ward of the current cannot change, this process would lead to a steep rise of the thermocline from the ocean toward the coast. Dashed line in the right panel marks the original position of the thermocline before uplift and orange circles denote the positions of strong current passing through (entering the paper).

geostrophic adjustment of the temperature field reacting to the presence of a strong current (see Fig. 7 and Tomczak and Godfrey (1994). Because isotherm depths on the offshore-ward side of the current cannot change, thus, this process would lead to a steep rise of the thermocline from the ocean toward the coast (Tomczak and Godfrey, 1994). Moreover, the uplifted subsurface cold water feeds in the cooling feature revealed in the SST (see Fig. 5c–5d). After 06:00 on July 29, the uplifted cold water falls down gradually back to deeper subsurface (see white arrows in Fig. 6e). Detailed cooling progress transects during the whole passage of Fungwong can be seen in animation A1 in SOM.

4. How fungwong triggers extreme cooling

4.1. Three-dimensional ocean state and its evolution: Control experiment

In this section, to further understand the exact mechanism(s) therein, the variations of three-dimensional velocity fields (u, v, w) and temperature during the entire typhoon passage at the Longdong site (centered at 25.08 °N, 122 °E) were examined. It is noting that the analysis was performed at the position of maximum surface cooling

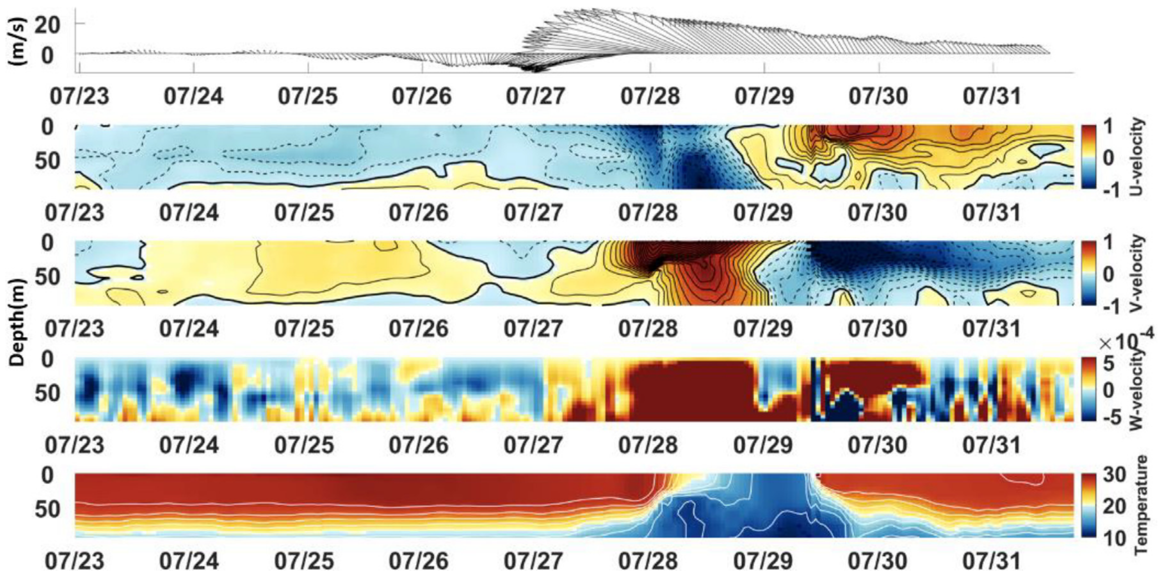

Fig. 8. Evolution of wind forcing (vectors), u, v, w-components of velocity fields (units, u: m s^{-1}, v: m s^{-1}, w: 10^{-4} m s^{-1}) and temperature (°C, color shading) are shown in panels from top to bottom. Model fields are sampled at 122 °E, 25.08 °N, which was chosen referring to where maximum sea surface cooling occurred. Positive values (contours in solid lines) in velocity fields correspond to eastward and northward flows for u and v, respectively. Contours in dashed lines in u and v fields denote negative, westward and southward velocities, respectively.

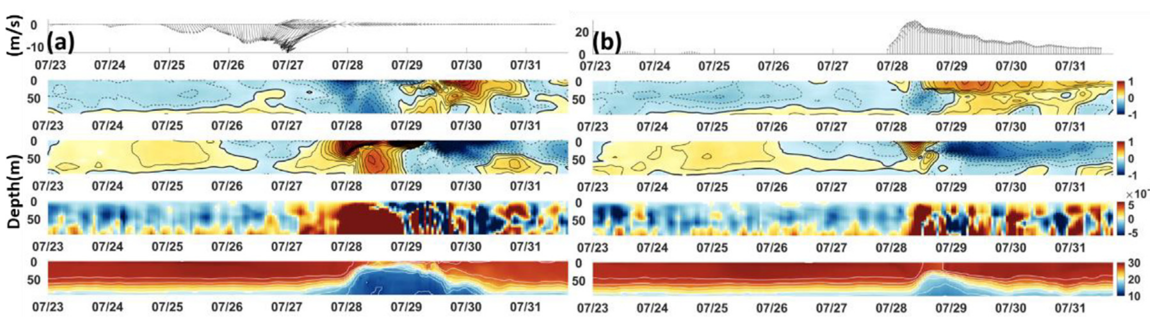

Fig. 9. Same as Fig. 8, but for the results from (a) EXP_{noSW} and (b) EXP_{SW}, respectively.

(25.08 °N, 122 °E) instead of exactly the position where buoy station deployed, because the dynamic analysis must capture the most active process located at corresponding area. By contrast, the temperature comparison was conducted exactly corresponding to the position of buoy station to provide a validation of the simulated temperature variations, since the buoy measured temperature was considered representative of a large amount of offshore water temperature (see animation A1 in SOM). This is the main reason why the analysis was performed slightly offshore relative to the temperature comparison corresponding to exactly the location of moored buoy. In Fig. 8, u-velocity shows a sudden and sharp shoreward shift from 18:00 on July 27 to 15:00 on July 28. Afterward, u-velocity changes to almost zero; a few hours later, the KMS starts to move offshore with an eastward velocity larger than 1 m s^{-1}. Meanwhile, with the shoreward shift of u-component velocity, the v-component velocity increases drastically to more than 1.3 m s^{-1}. This result implies that the KMS intrudes shoreward toward the Longdong in-situ measurement site. Subsequently, just behind the westward shift of the KMS, an extreme and rapid upwelling appeared from 00:00 on July 28 to almost 20:00 on July 28 (as shown in the w-component velocity field). Accordingly, a strong subsurface cooling originating from the deeper region (depth >=100 m) can be found immediately after the drastic upwelling from 00:00 on July 28. During this time, the uplifted subsurface cold water attains a depth of about 25 m and provides a favorable source of cold water for entrainment/vertical mixing (Price, 1981). Later, a strong temperature drop extends all the way to the sea surface. Meanwhile, the drop in temperature reaches up to approximately 15 °C relative to the state prior to the Fungwong passage. This result shows the important role of the uplift of the subsurface cold water in the response of extreme sea surface cooling to the Fungwong passage, as shown in the previous section. Nevertheless, the exact role of strong southerly winds (wind boost during 10:00–12:00 on 28 July) on the extreme cooling response to Fungwong remains unclear.

4.2. Experimental group

To further differentiate the effects of the shoreward intrusion of the Kuroshio and southerly wind on the uplift of subsurface cold water and thus the generation of the extreme cooling, here we conduct two additional experiments: (1) EXP_{noSW}: experiment using complete wind forcing but excluding southerly wind over the whole model domain and (2) EXP_{SW}: experiment using only southerly wind during the Fungwong passage. The difference between the three model experiments can be seen in Table 1. It should be noted that wind fields in those experiments are no longer physical. Fig. 9a shows the results of EXP_{noSW} simulation. Compared with the results of control simulation with complete dynamics (Fig. 8), EXP_{noSW} shows a similar pattern of Kuroshio intrusion but with slightly weaker strength. Without the contribution of southerly wind, it still leads to a sea surface cooling about 8 °C–9 °C, with similar pattern and timing as the cooling response simulated in the control experiment.

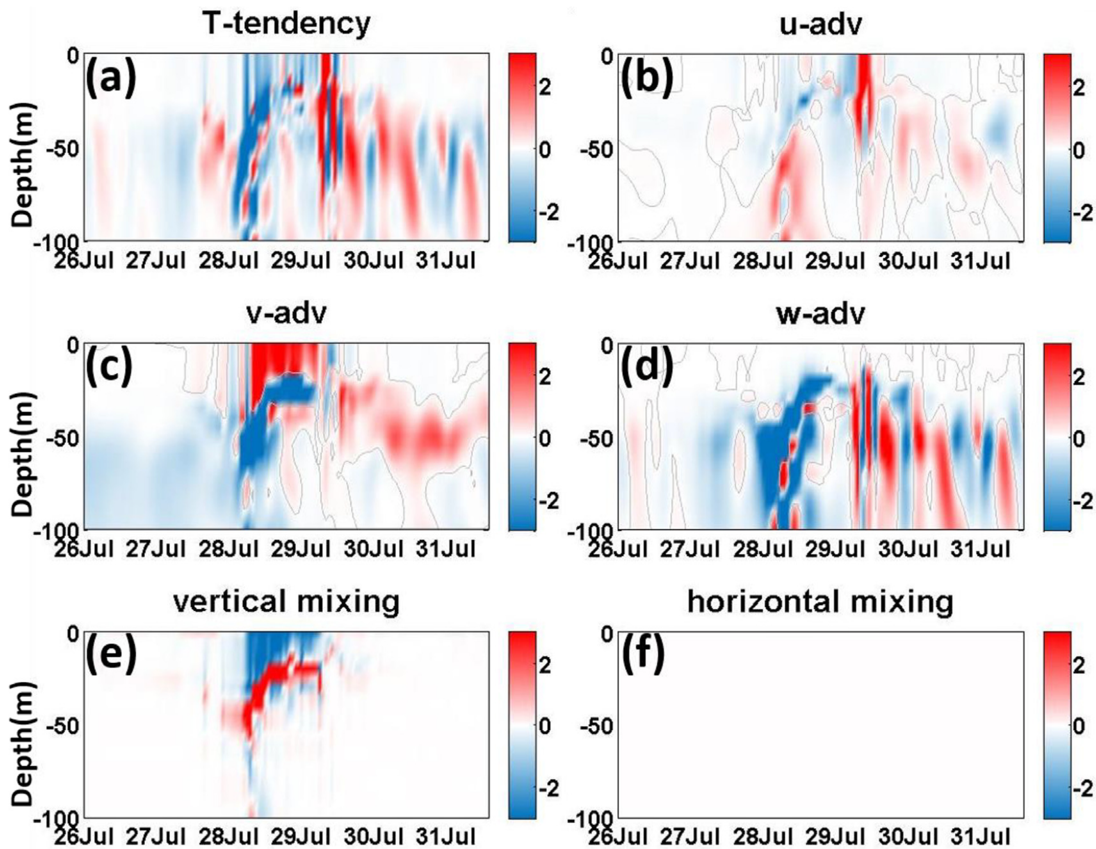

Fig. 10. Depth–time variations of each term (unit: 10^{-4} °C/second) in the conservation equation of the heat budget (Eq. (1)) for the model grid centered approximately closest to the maximum sea surface cooling (122 °E, 25.08 °N). The color shadings in blue (red) denote negative (positive) values. The gray solid contours denote zero values in u, v, and w-advection fields.

Fig. 9b shows the result of EXP_{SW}, which can be used to elucidate the role of southerly wind on the generation of extreme cooling to Fungwong. With only the influence of southerly wind and excluding the influence of northeasterly and easterly winds carried by the first-half passage of Fungwong, Kuroshio intrusion-like signals (e.g., negative u-velocity anomaly, sharp increase in positive v-velocity anomaly) are absent. Furthermore, the upwelling and consequential cooling largely decrease in comparison with either EXP_{noSW} or control simulation.

The results of these experiments clearly demonstrate that the southerly wind and consequential upwelling are not the main cause for triggering the extreme cooling to Fungwong. By contrast, the prior, stronger upwelling driven by the shoreward intrusion of the Kuroshio tied to easterly and northeasterly winds plays a dominant role. The comparison of results of EXP_{noSW} (Fig. 9a) to control experiment shows that the strong southerly wind plays a positive role in further enhancing the sea surface cooling. This result could be due to southerly wind enhancing entrainment mixing by injecting more momentum entering the upper ocean and mixing more uplifted cold water (~25 m depth) entering the mixed layer.

4.3. Heat budget analysis

The relationship between the dominant mechanisms triggering extreme cooling and consequential temperature variations were further examined by heat budget analysis following Glenn et al. (2016) and Kuo et al. (2018). The ROMS conservation of heat equation was used to quantify the relative contributions of the different terms responsible for the simulated distinctive sea surface cooling during the passage of Fungwong. The general conservation equation for the heat budget in ROMS is given below:

$$\overbrace{\frac{\partial T}{\partial t}}^{tendency} = \overbrace{-u\frac{\partial T}{\partial x} - v\frac{\partial T}{\partial y}}^{horizontal\ advection} - \overbrace{w\frac{\partial T}{\partial z}}^{vertical\ advection} + \overbrace{\frac{\partial}{\partial z}\left(k\frac{\partial T}{\partial z}\right)}^{vertical\ mixing} + \overbrace{D_T}^{horizontal\ mixing} + Residual \tag{1}$$

with the following vertical boundary conditions for surface (Eq. (2)) and bottom (Eq. (3)) respectively:

$$\left(k\frac{\partial T}{\partial z}\right)_{surface} = Q_{net}/\rho_0 C_P \tag{2}$$

$$\left(k\frac{\partial T}{\partial z}\right)_{z=-h} = 0 \tag{3}$$

where t is time, T is the temperature, u, v, w are the three-component of velocity. k is the vertical diffusivity coefficient; D_T is the horizontal mixing term. Q_{net} is the net surface heat flux, ρ_0 is density of seawater, C_p is the specific heat capacity of seawater and h is the depth.

Fig. 10 displays evolutions of separate terms in Eq. (1) from the surface to a depth of 100 m at the model grid closest to the maximum sea surface cooling (25.08 °N, 122 °E). It is noted that the net surface heat flux (Q_{net}) was included in the simulation in ROMS through the term of vertical diffusivity/mixing following the surface boundary condition of $\left(k\frac{\partial T}{\partial z}\right)_{z=0} = Q_{net}/\rho_0 C_P$ (Eq. (2)), as noted in both Hedstrom (2018) and Glenn et al. (2016). Thus, Q_{net} was not shown directly in the heat budget analysis (Fig. 10). More details about the temperature budget in ROMS can be seen in section of "ROMS heat balance analysis" in Glenn et al. (2016) and section of "Vertical boundary conditions (3.2)" in Hedstrom (2018). Here, residual is related to the slightly different temporal integrating intervals, time-varying vertical s-coordinate used in ROMS, and influence of friction (Glenn et al., 2016). In addition,

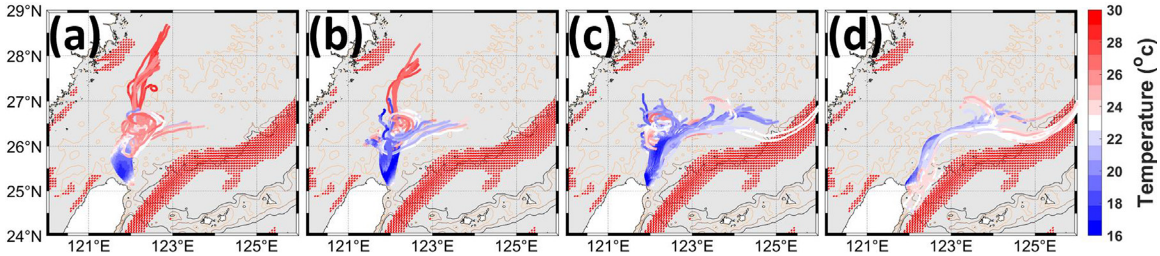

Fig. 11. ROMS modeled 7-days float trajectories with temperature variations since their releases. The floats were released along 25.09 °N (Fig. 1) during four stages of Fungwong passage: (a) 06:00–12:00 July 28, (b) 12:00–18:00 July 28, (c) 18:00–24:00 July 28 (d) 24:00 July 28–06:00 July 29. The red cross-hatched areas denote the regions of current speed stronger than 0.7 ms^{-1} (averaged of 21 to 25 July). Initial depths of the released floats are at 0.6 m below the sea surface. Corresponding depth variability of those modeled floats can be seen in Figure S3 in SOM.

the magnitude of the average residual in our analysis is ~5 × 10^{-5} (°C/s), which is approximately one order smaller than the other terms (except horizontal mixing). Fig. 10a shows the temperature rate of change, which is the sum of the zonal advection (Fig. 10b), meridional advection (Fig. 10c), vertical advection (Fig. 10d), and vertical mixing terms (Fig. 10e). Additionally, the horizontal mixing term (Fig. 10f) is close to zero and does not contribute to the rate of change of temperature.

As shown in Fig. 10a, a relatively marked decrease in surface mixed-layer temperature began at approximately 06:00 on July 28, showing consistent progress, as shown in two-dimensional sea surface cooling (Fig. 5c). The cooling tendency continued to almost 24 h till 06:00 on July 29, when it reached its lowest value. However, before the cooling tendency reached the sea surface, at approximately 00:00 on July 28, another cooling tendency originated from the deeper region (~100-m depth) and progressed all the way toward the sea surface with time. A few hours later, this cooling tendency originated from deeper layers combined with the prior cooling tendency of the shallow region (~0–25 m depth). According to temperature contributions by individual terms (Fig. 10b–10e), the influence of vertical advection ($w\frac{\partial T}{\partial z}$, occurred approximately at 19:00 on July 27) seems to dominate the cooling tendency originating from the deeper region. By contrast, the gradual uplift of deep cold water tied to vertical advection (upwelling) shows consistency with the uplift of cold water shown in transect plots (Fig. 6). Overall, during this period, the uplift of cold water from the deeper region provides a favorable cold-water source for later entrainment/vertical mixing associated with strong wind forcing carried by the Fungwong passage.

In the meantime, the variation of temperature in the upper ocean (~0–25 m depth) was due to the combined action of vertical advection and vertical mixing. The vertical mixing contributed to cooling in the mixed-layer but warming in the upper thermocline underlying strong wind forcing due to the process of mixed-layer deepening (Price, 1981). Generally, this would result in a cooler and thicker mixed layer. However, as shown in Fig. 10e, the upper thermocline rises and depresses the thickness of the mixed layer. The thermocline rising is attributed to the influence of the strong vertical advection of cold water. The continued supply of cold water from the deeper region would largely enhance the sea surface cooling through entrainment mixing. In the experiment of EXP$_{sw}$, the cooling tendency in the surface layer triggered by entrainment mixing is reduced to ~24% relative to control simulation forced using complete wind fields (calculated within 0–25 m). Again, this result confirms the key role of the uplift of subsurface cold water driven by the onshore intrusion of the Kuroshio on the generation of extreme cooling response to Fungwong passage.

5. Where the extremely cold water advects?

To track where the surface cold water advects in three dimensions, i.e., the sink of the extreme sea surface cooling water triggered by Fungwong, ROMS-modeled floats with temperature tracers were released over the region where maximum sea surface cooling occurred surrounding Longdong (see Fig. 1c and Fig. 5). The release period (from 06:00 on July 28 to 06:00 on July 29) is decided in accordance with the period of occurrence of maximum cooling (refer to Fig. 4). The initial depths of the released floats are 0.6 m below the sea surface.

Fig. 11 shows the trajectories of modeled floats along with their temperature variations (in color shadings). The individual float trajectories during different stages of release show how the cold water moves in response to the influences of strong wind forcing carried by Fungwong and the northward flowing Kuroshio Current. For the initial stage (Fig. 11a, showing trajectories of floats released during 06:00–12:00 on July 28), part of the floats drift northward due to the influence of strong southeasterly-southerly wind. Meanwhile, cold-water trajectories extend northward to about 200 km with temperature gradually recovering to the state of ambient waters. Subsequently, for the stages of floats encountering extreme cold waters (Fig. 11b–c), the direction of majority of the trajectories shifts gradually from north–northeast toward northeast. At this time, the cold-water trajectories with a temperature drop larger than 10 °C extend northward and northeastward over 300 km. Subsequently, with the diminishing strength of southerly wind, float trajectories bend to northeast–eastward toward the path of KMS (Fig. 11c–d); at this moment, the Kuroshio current gradually becomes the dominant forcing, determining the movement of most of the floats. Trajectories record cold waters extending more than 500 km with a temperature drop above 5 °C (Fig. 11d). Finally, floats with a temperature drop of more than 5 °C extend all the way eastward–northeastward toward the south end of Japan (Kyushu) along the Kuroshio downstream (Figure S4 in SOM).

All the floats released during the Fungwong passage can be separated into two main groups. The first group (accounting for ~58% of the total float trajectories) are those floats that move northward onto the ECS shelf that eventually mixes into deeper region (refer to the depth variability of all the modeled floats in Figure S3 in SOM) with slower movement due to the lack of energetic circulation over the shelf after typhoon passage. The other group of floats are those which get on the highway (KMS) and move eastward all the way with a higher velocity of about 1–1.5 m s^{-1}. This groups account for ~42% of the total trajectories. The second group of floats move eastward for about 600 km on the basis of the model simulation limited to a duration of 7 days.

To compare the difference of particle trajectories seeded from the extraordinary-cooled region (ECR) and the other regions, we conduct another online experiment with floats seeded at 0.5-degree east and 0.5-degree north of the original ECR, respectively. The results show interesting but unsurprising results, that is, for floats released east of the ECR, trajectories were advected along the KMS due to the influence of the Kuroshio current. By contrast, once the trajectories seeded 0.5-degree north of the ECR, majority of the trajectories were advected northward toward the ECS continent shelf (see Figure S5 in SOM).

As noted in previous studies, the transport of water with anomalous temperature differences is also responsible for unusual weather patterns, including surface winds, clouds, regional atmospheric circulation, and rainfall (e.g., (Barrick et al., 1977; Reason, 2001; Beal et al., 2011)). This finding implies that the far-reach effect of the extreme cooling response to TC passages, such as Fungwong, should not be overlooked. Nevertheless, the trajectories analysis was conducted on the basis of the currents provided by ROMS model simulation; characteristics revealed by the trajectories analysis must include errors because no model is perfect.

6. Summary

This study focused on an extreme SST drop of 12.5 °C in response to TC Fungwong (2008) passage, which was one of the strongest cooling responses recorded by historical in-situ instruments after a typhoon passage. On the basis of limited in-situ measurements of temperature, satellite-observed SST, and a suite of numerical experiments performed using ROMS, the detailed progress of how the Fungwong triggers such an extreme cooling were reproduced and systematically investigated. Source of the cold waters feeding the extreme cooling and possible mechanisms triggering the cooling, as well as consequential effects of extreme cooling on the surrounding oceanic environment, were unveiled. The major results are summarized as follows:

(1) The source of cold water feeding the extreme sea surface cooling in response to Fungwong is due mainly to the strong uplift of subsurface cold water near the coastal region tied to an onshore intrusion of the Kuroshio Current driven by easterly/northeasterly winds.
(2) Sensitivity experiments differentiated the effects of shoreward Kuroshio intrusion and the later southerly wind on the uplift of subsurface cold water. The shoreward Kuroshio intrusion plays a relatively dominant role on the generation of extreme cooling.
(3) Southerly wind plays a constructive role in the enhancement of entrainment mixing and thus sea surface cooling.
(4) Heat budget analysis explains the direct relationship between the possible mechanisms and consequential temperature variations.
(5) Overall, the extreme sea surface cooling response to Fungwong results mainly from a combined effect of prior uplift of subsurface cold water due to wind-driven onshore Kuroshio intrusion and later entrainment mixing partially enhanced by persistent southerly wind.
(6) Modeled float trajectories with temperature variations outline the affected region due to sharp sea surface cooling to Fungwong and indicate that the effect of cooling might extend all the way toward the south end of the Japan main island.

Previous studies indicated that the transport of water with anomalous temperature differences is responsible for unusual weather patterns (Barrick et al., 1977; Reason, 2001). Moreover, the effects of rapid decreases in water temperature on fish and aquaculture have also been well documented (Hoag, 2003; Troy et al., 2012). Our modeled float trajectories suggest that the corresponding effects resulting from the cold-water patches on the ECS continental shelf and far-field oceanic environment, ecological systems, weather patterns, and aquaculture may be important. The progress of the strong wind-driven onshore Kuroshio intrusion might lead to nutrient influx upward into the euphotic layer (e.g. Tsai et al. (2008)), which may consequently enter the ECS continental shelf. This process deserves the attention of biological, ecological, and geochemical researchers.

Declaration of competing interest

The authors declare that they have no known competing financial interests or personal relationships that could have appeared to influence the work reported in this paper.

Data availability

Data will be made available on request.

Table 1
List of model experiments in this study.

	Experiments	Descriptions
Control run	Fungwong (2008)	Forced by wind forcing and oceanic condition corresponding to Fungwong (2008)
Sensitivity-1	EXP_{noSW}	Experiment was driven by complete wind forcing but excluded southerly wind
Sensitivity-2	EXP_{SW}	Experiment was driven by southerly wind during the Fungwong passage only

Acknowledgments

This work is supported by National Science and Technology Council of Taiwan through grants of 108-2628-M-003-001-MY3 and 111-2611-M-003-003-MY3. The authors would like to thank the anonymous reviewers and editors for their very constructive comments. Their valuable comments and suggestions largely improve the presentation of this work. Thanks to NASA JPL (PO. DAAC), REMSS, GSFC, Central Weather Bureau (Taiwan), COMC(NCKU) scientific teams for processing and providing the essential data sets, as well as HYCOM and ROMS teams.

References

Babin, S.M., Carton, J.A., Dickey, T.D., Wiggert, J.D., 2004. Satellite evidence of hurricane-induced phytoplankton blooms in an oceanic desert. J. Geophys. Res. 109 (C03043), http://dx.doi.org/10.1029/2003JC001938.
Barrick, D.E., Evans, M.W., Weber, B.L., 1977. Ocean surface currents mapped by radar. Science 198 (4313), 138–144.
Beal, L., de Ruijter, W., Biastoch, A., et al., 2011. On the role of the Agulhas system in ocean circulation and climate. Nature 472, 429–436. http://dx.doi.org/10.1038/nature09983.
Brewin, R.J.W.L., de Mora, O., Billson, et al., 2017. Evaluating operational AVHRR sea surface temperature data at the coastline using surfers. Estuarine Coast. Shelf Sci. 196, 276–289.
Chin, T.M., Vazquez-Cuervo, J., Armstrong, E.M., 2017. A multi-scale high-resolution analysis of global sea surface temperature. Remote Sens. Environ. 200, 154–169. http://dx.doi.org/10.1016/j.rse.2017.07.029.
Cione, J., Uhlhorn, E., 2003. Sea surface temperature variability in hurricanes: Implications with respect to intensity change. Mon. Weather Rev. 131, 1783–1796.
Cummings, J.A., 2005. Operational multivariate ocean data assimilation. Q. J. R. Meteorol. Soc. 131, 3583–3604.
Donaldson, M.R., Cooke, S.J., Patterson, D.A., Macdonald, J.S., 2008. Cold shock and fish. J. Fish Biol. 73, 1491–1530.
Doong, D.-J., Peng, J.P., Babanin, A.V., 2019. Field investigations of coastal sea surface temperature drop after Typhoon passages. Earth Syst. Sci. Data 11, 323–340. http://dx.doi.org/10.5194/essd-11-323-2019.
Glenn, S.M., Miles, T.N., Seroka, G.N., Xu, Y., Forney, R.K., Yu, F., Roarty, H., Schofield, O., Kohut, J., 2016. Stratified coastal ocean interactions with tropical cyclones. Nature Commun. 7 (10887).
Hedstrom, K., 2018. Technical Manual for a Coupled Sea-Ice/Ocean Circulation Model (Version 5). U.S. Dept. of the Interior, Bureau of Ocean Energy Management, Alaska OCS Region. OCS Study BOEM 2018-2007, p. 182.
Hoag, H., 2003. Atlantic cod meet icy death. Nature 422 (792).
Ko, D.-S., Chao, S.-Y., Wu, C.-C., Lin, I.-I., Jan, S., 2016. Impacts of tides and Typhoon Fanapi (2010) on seas around Taiwan. Terr. Atmos. Ocean. Sci. 27, 261–280. http://dx.doi.org/10.3319/TAO.2015.10.28.01.
Kuo, Y.-C., Zheng, Z.-W., Zheng, Q., Gopalakrishnan, G., Lee, H.-Y., 2018. Typhoon-Kuroshio interaction in an air-sea coupled system: Case study of Typhoon nanmadol 2011. Ocean Model. 132, 130–138.
Kuo, Y.-C., Zheng, Z.-W., Zheng, Q., Gopalakrishnan, G., Lee, C.-Y., Chern, S.-W., Chao, Y.-H., 2017. Typhoon induced summer cold shock advected by Kuroshio off eastern Taiwan. Ocean Model. 109, 1–10. http://dx.doi.org/10.1016/j.ocemod.2016.11.003.
Large, W.G., McWilliams, J.C., Doney, S.C., 1994. Oceanic vertical mixing: A review and a model with a nonlocal boundary layer parameterization. Rev. Geophys. 32, 363–403.
Lee, C.-Y., Chen, S.S., 2014. Stable boundary layer and its impact on tropical cyclone structure in a coupled atmosphere-ocean model. Mon. Wea. Rev. 142, 1927–1944. http://dx.doi.org/10.1175/MWR-D-13-00122.1.
Lin, I.-I., Liu, W.T., Wu, C.-C., Wong, G.T.F., Hu, C., Chen, Z., Liang, W.-D., Yang, Y., Liu, K.-K., 2003. New evidence for enhanced ocean primary production triggered by tropical cyclone. Geophys. Res. Lett. 30 (13), 1718. http://dx.doi.org/10.1029/2003GL017141.

Lin, I.-I., Wu, C.-C., Pun, I.-F., Ko, D.-S., 2008. Upper-ocean thermal structure and the western north Pacific category 5 Typhoons. Part I: Ocean features and the category 5 Typhoons' intensification. Mon. Weather Rev. 136, 3288–3306.

Matthews, J.B.R., 2013. Comparing historical and modern methods of sea surface temperature measurement-part 1: review of methods, field comparisons and dataset adjustments. Ocean Sci. 9, 683–694. http://dx.doi.org/10.5194/os-9-683-2013.

Mohanty, S., Nadimpalli, R., Osuri, K.K., Pattanayak, S., Mohanty, U.C., Sil, S., 2019. Role of sea surface temperature in modulating life cycle of tropical cyclones over bay of Bengal. Trop. Cyclone Res. Rev. 8 (2), 68–83. http://dx.doi.org/10.1016/j.tcrr.2019.07.007.

Morimoto, A., Kojima, S., Jan, S., Takahashi, D., 2009. Movement of the Kuroshio axis to the northeast shelf of Taiwan during Typhoon events. Estuar. Coast. Shelf Sci. 82 (3), 547–552.

Price, J.F., 1981. Upper ocean response to a hurricane. J. Phys. Oceanogr. 11, 153–175.

Reason, C.J.C., 2001. Evidence for the influence of the Agulhas current on regional atmospheric circulation patterns. J. Clim. 14, 2769–2778.

Schade, L.R., Emanuel, K.A., 1999. The ocean's effect on the intensity of tropical cyclones: Results from a simple coupled atmosphere ocean model. J. Atmos. Sci. 56, 642–651.

Shay, L.K., Goni, G.J., Black, P.G., 2000. Effects of a warm oceanic feature on Hurricane Opal. Mon. Weather Rev. 128, 1366–1383.

Shchepetkin, A.F., McWilliams, J.C., 2003. Method for computing horizontal pressure-gradient force in an oceanic model with a nonaligned vertical coordinate. J. Geophys. Res. 108 (C3), 3090. http://dx.doi.org/10.1029/2001JC001047.

Shchepetkin, A.F., McWilliams, J.C., 2005. The regional oceanic modeling system (ROMS): A split-explicit, free-surface, topography-following-coordinate oceanic model. Ocean Modell. 9, 347–404.

Shen, D., Li, X., Wang, J., Bao, S., Pietrafesa, L.J., 2021. Dynamical ocean responses to Typhoon Malakas 2016 in the vicinity of Taiwan. J. Geophys. Res. 126, http://dx.doi.org/10.1029/2020JC016663, e2020JC016663.

Siswanto, E., Ishizaka, J., Yokouchi, K., Tanaka, K., Tan, C.K., 2007. Estimation of interannual and interdecadal variations of Typhoon-induced primary production: A case study for the outer shelf of the east China sea. Geophys. Res. Lett. 34 (L03604), http://dx.doi.org/10.1029/2006GL028368.

Smith, W.H.F., Sandwell, D.T., 1997. Global seafloor topography from satellite altimetry and ship depth soundings. Science 277, 1957–1962.

Song, Y., Haidvogel, D.B., 1994. A semi-implicit ocean circulation model using a generalized topography-following coordinate system. J. Comput. Phys. 115 (1), 228–244.

Tomczak, M., Godfrey, J.S., 1994. Regional Oceanography: An Introduction. Elsevier, Amsterdam, The Netherlan7ds.

Troy, C.D., Ahmed, S., Hawley, N., Goodwell, A., 2012. Cross-shelf thermal variability in southern lake Michigan during the stratified periods. J. Geophys. Res. 117 (C02028), http://dx.doi.org/10.1029/2011JC007148.

Tsai, Y., Chern, C.-S., Wang, J., 2008. Typhoon induced upper ocean cooling off northeastern Taiwan. Geophys. Res. Lett. 35 (L14605), http://dx.doi.org/10.1029/2008GL034368.

Woo, H.-J., Park, K.-A., 2020. Inter-comparisons of daily sea surface temperatures and in-situ temperatures in the coastal regions. Remote Sens. 12 (1592), http://dx.doi.org/10.3390/rs12101592.

Wu, C.-C., Lee, C.Y., Lin, I.I., 2007. The effect of the ocean eddy on tropical cyclone intensity. J. Atmos. Sci. 64, 3562–3578.

Zheng, Z.-W., Ho, C.-R., Zheng, Q., Kuo, N.-J., Lo, Y.-T., 2010. Satellite observation and model simulation of upper ocean biophysical response to super Typhoon Nakri. Cont. Shelf. Res. 30 (13), http://dx.doi.org/10.1016/j.csr.2010.05.005.

Zheng, Z.-W., Lin, I.-I., Wang, B., Huang, H.-C., Chen, C.-H., 2015. A long neglected damper in the El Nino-Typhoon relationship: A gaia-like process. Sci. Rep. 5 (11103), http://dx.doi.org/10.1038/srep11103.

Zheng, Z.-W., Zheng, Q., Gopalakrishnan, G., Kuo, Y.-C., Yeh, T.-K., 2017. Response of upper ocean cooling off northeastern Taiwan to Typhoon passages. Ocean Model. 115, 105–118. http://dx.doi.org/10.1016/j.ocemod.2017.05.008.

Zheng, Z.-W., Zheng, Q., Lee, C.-Y., Gopalakrishnan, G., 2014. Transient modulation of Kuroshio upper layer flow by directly impinging Typhoon Morakot in east of Taiwan in 2009. J. Geophys. Res. Oceans 119, 4462–4473. http://dx.doi.org/10.1002/2014JC010090.